

The effect of cation-disorder on lithium transport in halide superionic conductors

Peichen Zhong,^{1,2} Sunny Gupta,^{1,2} Bowen Deng,^{1,2} KyuJung Jun,^{1,2} and Gerbrand Ceder^{1,2,*}

¹*Department of Materials Science and Engineering,*

University of California, Berkeley, California 94720, United States

²*Materials Sciences Division, Lawrence Berkeley National Laboratory, California 94720, United States*

(Dated: March 14, 2024)

Among the chloride-based Li-ion solid electrolytes, Li_2ZrCl_6 (LZC) have emerged as potential candidates due to their affordability, moisture stability, and high ionic conductivity. LZC synthesized by solid-state heating exhibits limited Li-ion conductivity while the mechanochemical ball-milled material is more conductive. In this computational study, we integrate thermodynamic modeling, using cluster-expansion Monte Carlo, and kinetic modeling, using molecular dynamics, to investigate whether cation disorder can be achieved in LZC, and how it affects Li-ion transport. Our results indicate that fast Li-ion conductivity is induced by the activation of Li/vacancy disorder, which itself depends on the degree of Zr disorder. We find that the very high-temperature scale at which equilibrium Zr-disorder can form precludes any equilibrium synthesis processes for achieving fast Li-ion conductivity, rationalizing why only non-equilibrium synthesis methods, such as ball milling leads to good conductivity. We identify as the critical mechanism the lack of Li/vacancy disorder near room temperature when Zr is well-ordered. Our simulations further show that the Li/vacancy order-disorder transition temperature is lowered by Zr disorder, which is necessary for creating high Li diffusivity at room temperature. The insights obtained from this study raise a challenge for the large-scale production of these materials and the potential for the long-term stability of their properties.

I. INTRODUCTION

High-Li-ion-conductivity solid electrolytes are essential for realizing all-solid-state batteries (ASSBs), which offer the potential for increased volumetric energy density and improved safety compared to conventional liquid-electrolyte-based batteries [1–3]. Chloride-based Li-ion solid electrolytes, with the general formula $\text{Li}_x\text{M}_y\text{Cl}_6$, where M represents a transition metal and in which Cl anions form a close-packed framework, have become of interest as catholytes in ASSBs [4–10]. Many of these electrolytes exhibit high room-temperature (RT) Li-ion conductivity (> 1 mS/cm), good interfacial stability with cathode materials, and high oxidation stability [5, 9, 11–13], consistent with early theory predictions [14]. Significant challenges still exist before these materials can be commercialized in practical cells. Some of the halide conductors contain low-abundance metals (e.g., Sc/Y/Tb/Lu). In addition, many of the interesting halides are unstable in ambient conditions and their ionic conductivity significantly degrades by exposure to moisture [4, 15]. Recently, the Zr-based compounds (e.g., Li_2ZrCl_6 , LZC) and their doped variants have demonstrated the potential to overcome these challenges [7, 16–22]. LZC exhibits distinct polymorphism with its structure depending on the synthesis method as summarized in Fig. 1(a). Mechanochemical synthesis produces α_h -LZC (hexagonal close-packed anions, hcp), whereas the β_c -LZC (cubic close-packed anions, ccp) can form by annealing α_h -LZC at temperatures above 260 °C (see Fig. 1(a)). While the ball-milled α_h -LZC exhibits

RT Li-ion conductivity of approximately 0.8 mS/cm [16], the annealed LZC in either the α - or β -phase display significantly lower RT Li-ion conductivity [16]. This has led to the hypothesis that some disorder is critical to achieve high ionic conductivity. Mechanochemical ball-milling as a non-equilibrium synthesis method is capable of inducing high-energy cation-disordered configurations [23, 24]. Schlem *et al.* [25] demonstrated that in Li_3YCl_6 and Li_3ErCl_6 mechanochemical synthesis induces cation defects by creating disorder on the sites occupied by Y/Er and that this results in a reduced activation energy and enhanced ionic conductivity. Using molecular dynamics simulations, Wang *et al.* [26] revealed that the Li sublattice disorders above $T_c = 425$ K in Li_3YCl_6 , and that the associated broadening of the Li site energies creates fast Li-ion diffusion. Other approaches such as introducing stacking faults [27] and tuning Li/metal stoichiometry to create percolation pathways [28, 29] have also been proven to enhance Li-ion conductivity.

In this study, we seek to explain the correlation between synthesis route, cation disorder, and ion transport in LZC systems through *ab initio* modeling. Using cluster-expansion Monte Carlo (CE-MC) simulations for both α - and β - phases, we demonstrate that, in equilibrium, Li- and Zr-disorder occur at very different temperatures. Our results suggest that facile Li disorder only emerges at room temperature in the presence of Zr disorder, but that equilibrium Zr disorder only occurs at very high temperatures. In the low-temperature equilibrium states in which Zr is well-ordered, Li/vacancy intersite exchanges are thermodynamically limited, leading to very low conductivity. The finding that at low temperature Li disorder is driven by Zr disorder is further confirmed by molecular dynamics (MD) simulations

* gceder@berkeley.edu

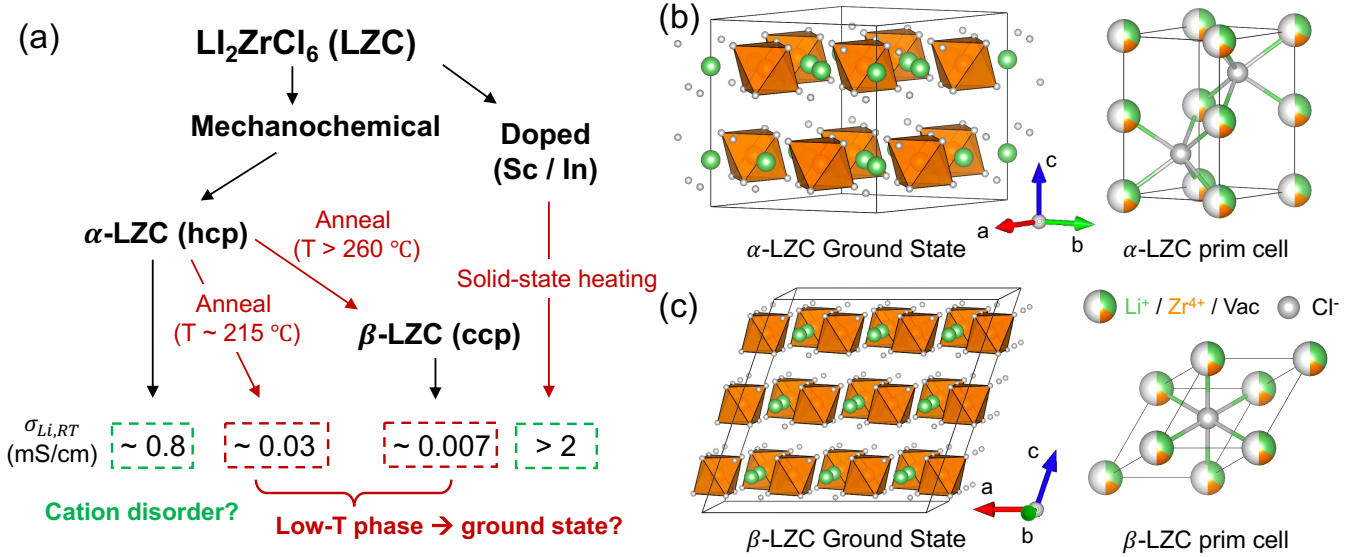


FIG. 1. (a) A summary of the synthesis paths and ionic conductivities of LZCs. (b) An illustration of the ground-state structure and primitive cell used for lattice models (b) α -LZC (hcp) and (c) β -LZC (fcc). The green/orange/white balls represent the cation site that can be occupied by Li/Zr/vacancies, respectively. The grey ball represents the anion site with Cl occupancy.

using machine-learning interatomic potentials, in which we find a significant improvement in Li ionic diffusivity with the presence of Zr disorder. Our investigation demonstrates that Zr disorder is essential to achieve high Li conductivity, but cannot likely be achieved through thermal equilibrium synthesis routes, thereby explaining why extensive ball milling is required for these materials. We believe this to be a challenge for the large-scale production of these materials as well as a potential problem for the long-term stability of their properties.

II. METHODS

A. Cluster expansion

The cluster-expansion (CE) method [30] is used to study the configurational thermodynamics of materials in which sites can be occupied by multiple cations, and has been applied to study the Li-vacancy intercalation chemistry in layered and disordered materials [31, 32] as well as solid electrolytes with Li/vacancy disorder [33, 34]. The CE expands the energy as a sum of many-body configurational interactions:

$$E(\boldsymbol{\sigma}) = \sum_{\beta} m_{\beta} J_{\beta} \langle \Phi_{\alpha \in \beta} \rangle_{\beta} + \frac{E_0}{\epsilon_r}, \quad \Phi_{\alpha} = \prod_{i=1}^N \phi_{\alpha_i}(\sigma_i) \quad (1)$$

A configuration $\boldsymbol{\sigma}$ represents a specific occupancy state of species its allowed sites, and σ_i describes which species sit on the i -th site of the lattice. The cluster basis function $\Phi_{\alpha} = \prod_{i=1}^N \phi_{\alpha_i}(\sigma_i)$ is the product of site basis functions

$\phi_{\alpha_i}(\sigma_i)$ across a collection α of multiple sites. The average is taken over the crystal symmetry orbits β , forming a complete basis to expand the energy function in the configuration space. The expansion coefficients J_{β} are called effective cluster interactions (ECIs). The electrostatic energy (Ewald energy E_0/ϵ_r) is included to capture long-range electrostatic interactions (E_0 is the unscreened electrostatic energy, and $1/\epsilon_r$ is fitted as one of the ECIs).

The CEs of LZC were performed with pair clusters up to 8 Å, triplet clusters up to 5 Å, and quadruplets up to 5 Å using a hcp primitive cell based on the unit cell of Li_3YCl_6 (ICSD-29962) for α -LZC, and with pairs up to 10 Å, triplets up to 7 Å, and quadruplet interactions up to 4 Å using a fcc primitive cell based on the unit cell of Li_3InCl_6 (ICSD-17638) for β -LZC (see Fig. 1). Occupancy of the metal sites is restricted to $\text{Li}^+/\text{Zr}^{4+}/\text{vacancy}$ in the CEs. In total, 104/70 ECIs (including the constant term J_0) were defined, and the CEs for the MC simulations were fitted with the energies of 528/568 different structures for α/β -LZC, where 62/82 structures were directly relaxed using $r^2\text{SCAN}$ density functional theory (DFT) calculations, and the energy of the remaining structures was determined by CHGNet through the ground-state determination procedure described below. When CHGNet is tested on the DFT relaxed structures, a root-mean-squared error of 8 meV/Cl is achieved. Although the CHGNet energy is not as accurate as the direct DFT value, we find that the CHGNet error is similar to the CE fitting error (< 7 meV/Cl). It is noted that this is a typical error scale for describing the configurational disorder as reported in several reported solid-state systems [35]. An $\ell_0\ell_2$ -norm regularized

regression with ground-state preservation algorithm was applied when fitting the ECI to address the complexity-induced over-fitting [36, 37]. Gurobi was used as the optimizer [38]. We refer the readers to Ref. [39] for detailed formalism and terminology of the CE. The ECIs were parameterized with root-mean-squared errors < 7 meV/Cl for both the α - and β -CEs. The CE constructions were performed using `smol` [40] and `pymatgen` for structure processing [41].

B. Ground-state determination

The ground-state (GS) determination identifies the metal configuration with the lowest energy among all possible configurations on the partially occupied lattice. To efficiently accomplish this task, we relied on the Crystal Graph Hamiltonian Neural Network (CHGNet) to relax structures and evaluate their energy [42]. The CHGNet was fine-tuned on a dataset in the Li-Zr-Cl chemical space, which is composed of DFT structure relaxation trajectories of LZCs, LiCl, and ZrCl₄ (approximately 19,000 atomic configurations). The different Li/Zr/vacancy orderings in LZCs were generated using the enumeration method (`OrderDisorderedTransformation`) in `pymatgen` [41]. CHGNet achieves mean absolute errors of 6 meV/atom for energy, 11 meV/Å for interatomic forces, and 0.011 GPa for stress on the validation set. To find the ground state of LZC, we implemented a GS search workflow, which is composed of the following steps. (1) Fitting a CE Hamiltonian using the CHGNet-relaxed structures as a training set, which is obtained by collecting the relaxed structures from step (3) cumulatively as the iteration proceeds (random values of ECIs were initialized in the first iteration); (2) running simulated annealing with canonical MC to search for any structure with lower energy compared to the existing CE training set; (3) Each such structure was relaxed using CHGNet and added to the set of structures to which the CE is fitted, after which all steps were repeated from (1). The workflow was fully automated until no new GS was detected. After that, the 50 structures with the lowest energy from the CHGNet predictions were relaxed with DFT. The ground state ordering was determined to be the structure with the lowest DFT energy.

DFT calculations were performed using the regularized strongly constrained and appropriately normed meta-GGA exchange-correlation functional (r²SCAN) [43, 44], as implemented in the *Vienna ab initio simulation package* (VASP) using the projector-augmented wave method [45, 46], a plane-wave basis set with an energy cutoff of 680 eV and a reciprocal space discretization of 25 k -points per Å⁻¹. The calculations were converged to 10⁻⁶ eV in total energy for electronic loops and 0.02 eV/Å in interatomic forces for ionic loops.

C. Monte Carlo simulations

Equilibrium metal disorder at finite temperatures can be studied by MC simulations on the CE Hamiltonian. These MC simulations were performed in the canonical ensemble by heating from the identified GS (see Fig. 1(b)-(c)) at $T = 0$ K to 5000 K with a temperature step of $\Delta T = 50$ K. At each temperature step, a total of 200 structures were uniformly sampled from 2,000,000 configurations obtained in the canonical equilibrium ensemble after equilibration at each T_{eff} with 200,000 MC steps. The structures sampled from the equilibrium ensemble were used to calculate the average energy $\langle E \rangle$ and the heat capacity $C_v = \sigma^2(E)/k_B T^2$, $\sigma^2(E) = \langle E^2 \rangle - \langle E \rangle^2$ is the energy fluctuation. Randomly picked MC structures from the equilibrium ensembles at different T_{eff} were selected to study the equilibrium Li/vacancy disorder for fixed Zr occupancies. In these simulations, the Zr disorder from the MC state obtained at T_{eff} is frozen but the Li/vacancy configuration is equilibrated from T_{eff} to 0 K with a temperature step of $\Delta T = -50$ K.

D. Machine-learning interatomic potentials for molecular dynamics

Recent developments of machine-learning interatomic potentials (MLIP) [47, 48] have enabled large-scale and nano-second-long simulations to directly simulate the Li transport kinetics near room temperature [49]. We used CHGNet to implement MLIP-MD. CHGNet was fine-tuned with *ab-initio* calculations in the generalized gradient approximation (GGA) functional [50] as described below. The DFT calculations were performed with VASP using Gamma-point-only for k -space sampling and a plane-wave energy cutoff of 500 eV. Large supercells with cell lengths of at least 10 Å in each direction were used. The calculations were converged to 10⁻⁶ eV in total energy and the DFT-D3 method of Grimme was used to include Van der Waals corrections [51].

The training set to fine-tune CHGNet for MD simulations was created through the following steps. (1) Three cation configurations with different Zr disorder were taken from MC simulations with $T_{\text{eff}} = 0/3050/5000$ K and annealed down to 0 K in MC to equilibrate the Li/vacancy configuration. This was performed for both α - and β -LZC and the resulting structures were relaxed with DFT calculations using the GGA-D3 functional. (2) Five different configurations were generated by applying strains (-1%, 0%, +1%, +2%, +3%) to these DFT-relaxed structures. (3) We used Bayesian force fields implemented in the `Flare` package to sample the atomic configurations with on-the-fly (OTF) MD [52, 53]. The DFT calculation was called when the uncertainty threshold is higher than `std_tolerance_factor=-0.03` in `Flare`. OTF-MD in the NVT ensemble was initiated from each strained configuration by heating from 0 K to the target temperatures ($T = 300/400/600/800$ K) using

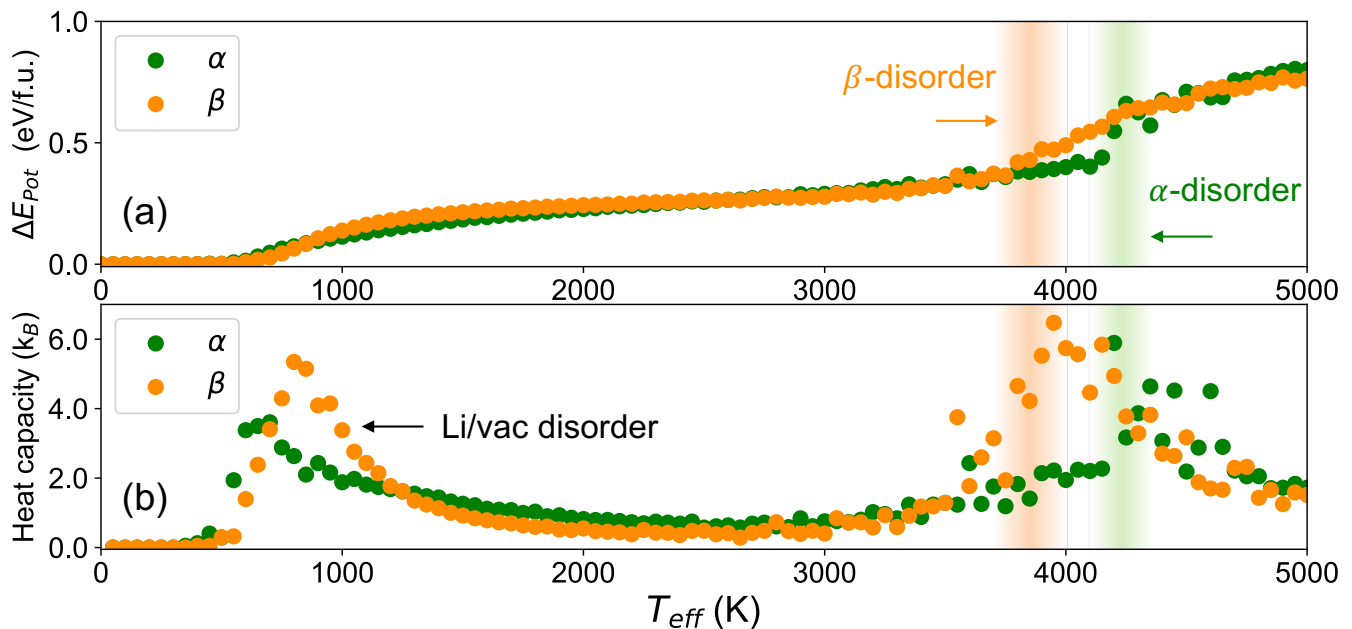


FIG. 2. (a) The average potential energy above the ground state ($\Delta E = E(T_{\text{eff}}) - E_{\text{GS}}$) sampled full equilibrium CE-MC simulations. The green/orange dots represent α/β -LZC, respectively. The shaded regions label the increase of potential energy as an indication of the Zr disorder. (b) The calculated heat capacity C_v . The first rise in C_v corresponds to the transition to Li/vacancy disorder, and the second rise (indicated by the shaded region) corresponds to the transition where Zr disorders.

the Berendsen thermostat [54]. For each MC configuration, a total of 20 OTF-MD simulations were conducted in parallel, covering five different strains at four distinct temperatures. (4) After the OTF-MD sampling, we fitted a trial CHGNet to initiate NPT-MD simulations of up to 50 ps starting from the DFT-relaxed structures. The MD trajectories were randomly sampled and the energy of these configurations, calculated with static DFT, was added to the MLIP training set (approximately 10,000 structures). In total, over 18,000 atomic configurations and their DFT energy were used to fine-tune the pre-trained CHGNet for MD production. The final CHGNet model (for MD simulations) achieves mean absolute errors of 1 meV/atom for energy, 34 meV/Å for interatomic forces, and 0.021 GPa for stress on the validation set.

The MD simulations to obtain Li diffusivity were initiated from the DFT-relaxed structures with a 50-ps initial equilibration in the NPT ensemble. The output of these short simulations was used to initiate longer MDs in the NVT ensemble for production. The Li self-diffusion coefficients were obtained by calculating the mean squared displacements of Li trajectories for at least 2 ns. The diffusivity and activation energy were computed following the empirical error estimation scheme proposed by He *et al.* [55]. All the MD simulations were implemented using the Atomic Simulation Environment (ASE) interface [56].

III. RESULTS

A. Cation disorder at elevated temperatures

To investigate the thermodynamics of cation disorder in LZCs, we conducted CE-MC simulations to sample the average and fluctuation of the configurational energy at finite temperatures. Figure 2(a) presents the average potential energy above the ground state $\Delta E_{\text{pot}} = E(T_{\text{eff}}) - E_{\text{GS}}$, and Fig. 2(b) shows the heat capacity $C_v = \sigma^2(E)/k_B T^2$, where the green/orange dots represent α/β -LZC, respectively.

The two significant increases in ΔE_{pot} accompanied by peak signals in C_v for both α/β -LZC indicate order-disorder phase transitions. The heat capacity peak near 500 K is associated exclusively with Li/vacancy disorder, and no Zr disorder is detected in the MC structures in this temperature range. The subsequent increase in ΔE_{pot} and corresponding peak in C_v near 4000 K corresponds to the Zr order-disorder phase transition, which is marked by the green/orange shaded region in Fig. 2. Such a high temperature suggests that there is no spontaneous Zr disorder from thermal fluctuations at the typical temperatures accessible to solid-state synthesis. Given these results, it is clear that only high-energy, non-equilibrium synthesis approaches such as mechanochemical ball-milling can achieve the disordered state.

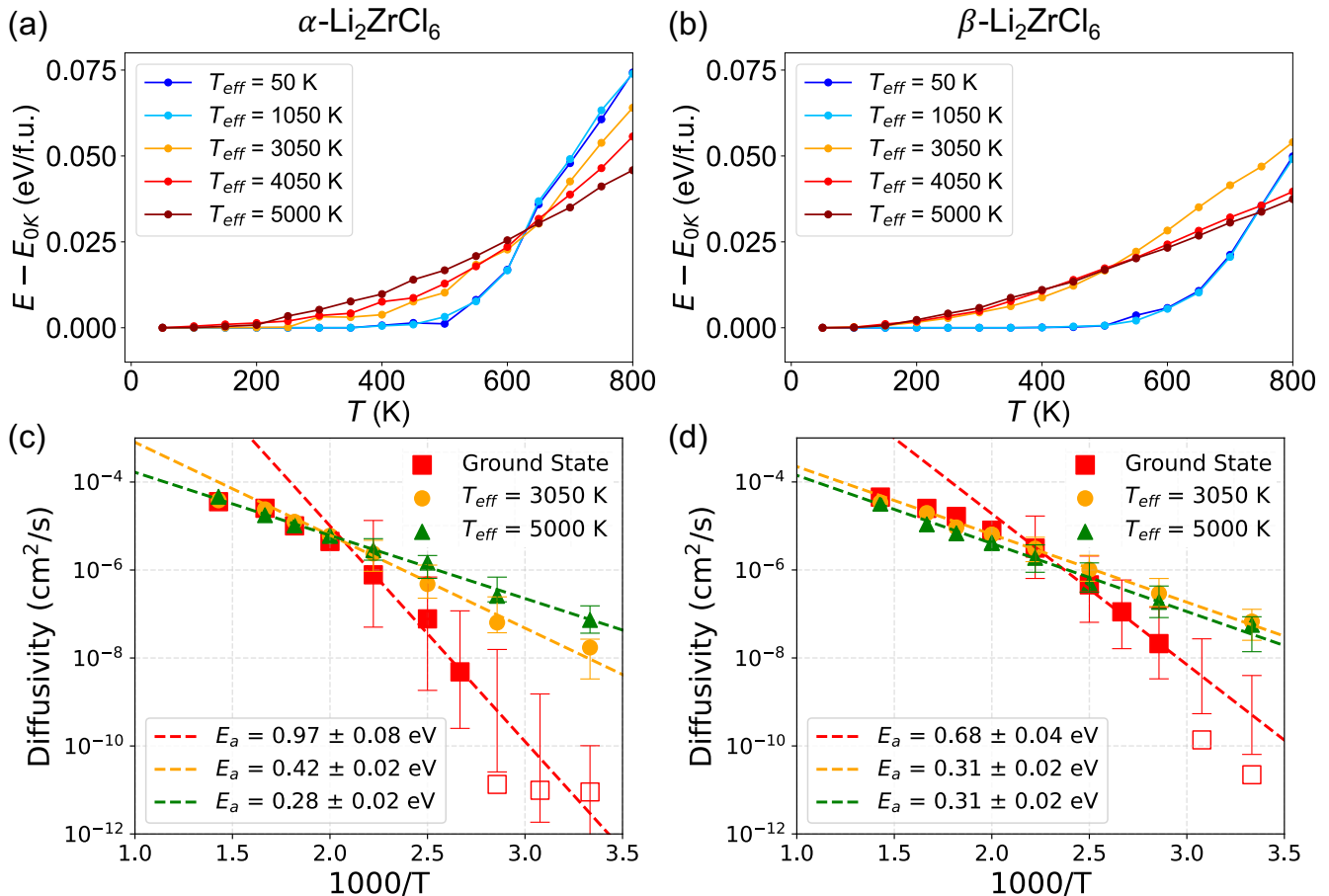


FIG. 3. (a)-(b) The Li/vacancy configurational energy landscape $\{E_T\}$ sampled by MC annealing with fixed Zr ordering. The color lines represent the average energy sampled by the Li/vacancy degrees of freedom with various Zr orderings obtained by equilibration at T_{eff} . The rise in $\{E_T\}$ indicates the activation of Li/vacancy inter-site exchanges (disorder). As the T_{eff} at which the Zr was disordered increases, Li can more easily sample higher energy states. (c)-(d) Arrhenius plots of the MD simulated diffusivities *vs.* temperature from 300 K to 700 K. The MD simulations started from the Zr configurations obtained with MC at $T_{\text{eff}} = 0$ K (green triangles), 3050 K (orange dots), and 5000 K (red squares). The dashed lines represent the activation energy fitted in the low-temperature range ($T < 500$ K). A significant non-Arrhenius behavior is observed in Li diffusion in the ground-state structure. The presence of Zr disorder reduces the degree of non-Arrhenius behavior, and the dashed line fitted in low-temperature regions extends well to the high-temperature region.

B. Li-site disorder conditioned on Zr orderings

To evaluate how the Li/vacancy site distribution is affected by the presence of Zr disorder, we investigated the energy sampled by the Li/vacancy configurations in a MC simulation when Zr ordering is fixed to that obtained at elevated temperatures. Figure 3 (a)-(b) shows the average configurational energy, $\{E_T\}$, sampled by the Li/vacancy degrees of freedom conditioned on various fixed Zr states of disorder (represented by T_{eff} , which is the temperature at which the Zr configurations were obtained). The x -axis represents the temperature at which the Li/vacancy energy was sampled in MC, and the y -axis shows the average energy difference above the 0 K configuration. The Li/vacancy energetics for both α - and β -LZC with $T_{\text{eff}} = 50$ K and 1050 K are almost the same, in-

dicating no Zr disorder occurs in this temperature range. When Zr is well ordered ($T_{\text{eff}} = 50$ K or $T_{\text{eff}} = 1050$ K), the Li/vacancy disorder initiates at approximately 500 K indicated by the characteristic potential-energy increase.

For the structures with a high degree of Zr disorder (e.g., $T_{\text{eff}} = 5000$ K), Li already samples higher-energy configurations at low temperatures (200 to 300 K) and no distinct order-disorder transition is observed, consistent with findings in other materials with coupled disorder [57]. This observation indicates that Li/vacancy configurational disorder at room temperature is made possible by Zr disorder.

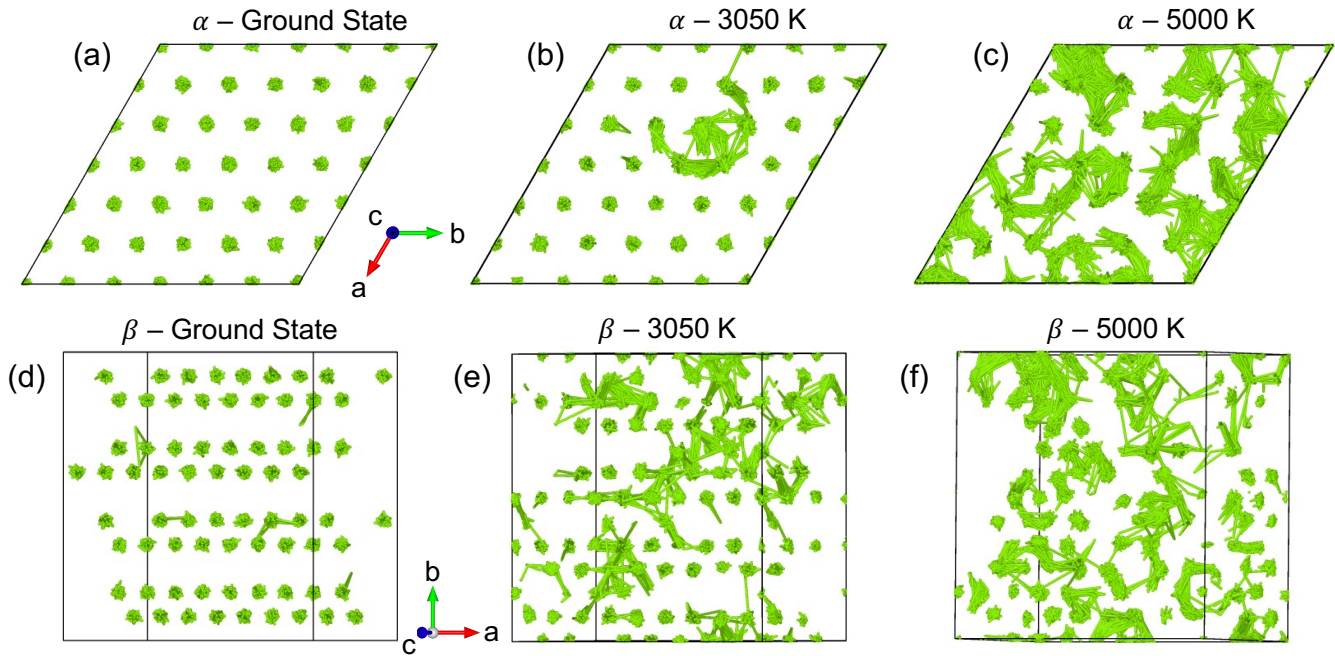


FIG. 4. The room-temperature Li diffusion trajectories from the MD simulations in (a)-(c) α -LZC and (d)-(f) β -LZC. The different degrees of Zr disorder are indicated by the effective temperatures with which they are obtained in MC.

C. Li transport as a function of Zr disorder

To obtain quantitative measures of Li diffusivity as a function of Zr disorder, we used MLIPs to run large-scale and long-time MD simulations. Structures with partial Zr disorder were obtained from MC simulations at $T_{\text{eff}} = 0/3050/5000$ K. In the MD simulations, Zr ions do not migrate so Li diffusion can be studied for a fixed Zr disorder. Figure 3(c)-(d) displays the Li diffusivities at temperatures from $T = 300$ K to 700 K in these structures. The ground-state structures (no Zr disorder) are represented by red squares, structures with partial Zr disorder ($T_{\text{eff}} = 3050$ K) are represented by orange dots, and structures beyond the Zr order-disorder transition ($T_{\text{eff}} = 5000$ K) are represented by green triangles. The dashed lines in Fig. 3(c)-(d) are fits to the activation energies using the diffusivities obtained from the low-temperature range (< 500 K). The unfilled squares represent diffusivities for which a limited amount of Li hopping is observed in the MD simulations leading to high error bars on the diffusivity (see Fig. 4(a) and (d) as examples).

For structures beyond the Zr order-disorder transition ($T_{\text{eff}} = 5000$ K, green triangles), the dashed line fit from the low-temperature region closely aligns with the high-temperature simulated diffusivities (500 K to 800 K), which indicates that the diffusion coefficient satisfies a simple Arrhenius law over the full temperature region. In contrast, structures without Zr disorder (ground state, red squares) exhibit marked non-Arrhenius behavior for both α - and β -LZC, as they show no overlap between

the dashed lines and high-temperature diffusivities. The steep slope of these red dashed lines indicates high activation energies near room temperature ($E_a = 0.97 \pm 0.08$ eV for α -LZC and $E_a = 0.68 \pm 0.04$ eV for β -LZC), significantly larger than those determined by nudged-elastic band (NEB) calculations within the hcp and ccp halide framework [12]. The analysis derived from MD simulations aligns closely with the thermodynamic data. The non-Arrhenius behavior of Li transport in the structures with ground-state Zr ordering arises from the order-disorder transition of Li and vacancies near 500 K (see blue lines in Fig. 3(a)-(b)), whereas such a transition is not observed for Zr-disordered structures.

The α - and β -LZC polymorph show distinct behavior when Zr is partially disordered ($T_{\text{eff}} = 3050$ K, orange dots in Fig. 3(c)-(d)). The diffusivity of Li in α -LZC with $T_{\text{eff}} = 3050$ K has an activation energy $E_a = 0.42 \pm 0.02$ eV, which is in between that of the ground state ordering and fully disordered Zr. In contrast, for β -LZC, Li diffusion for partial Zr disorder ($T_{\text{eff}} = 3050$ K) occurs with a similar activation energy than in the highly disordered case ($E_a = 0.31 \pm 0.02$ eV), suggesting that the ccp structures are conducive to Li diffusion even when Zr is only partially disordered. We find that the difference of activation energy in α and β -LZC is also reflected in the energy landscape, with α -LZC showing some flattening of the energy landscape (orange line in Fig. 3(a)). This mirrors the higher activation energy ($E_a = 0.42$ eV) as compared to the fully Zr-disordered state ($E_a = 0.28$ eV), as shown in Fig. 3(c). In contrast, the energy landscape for β -LZC (orange line in Fig. 3(b)) closely re-

sembles that of fully-disordered states (dark-red lines in Fig. 3(b)), consistent with the MD findings that suggest similar activation energies ($E_a = 0.31$ eV) for the two degrees of Zr disorder in β -LZC.

An illustration of the difference in the Li-transport kinetics is demonstrated in Fig. 4, where the Li diffusion paths in MD simulations are plotted. Very limited movement of Li ions is observed within the Zr ground state structures, as the Li-ions oscillate around their equilibrium sites (see Fig. 4(a) and (c)). At $T_{\text{eff}} = 3050$ K, limited Li hops to nearest sites are observed for α -LZC due to the partial Zr disorder, whereas β -LZC shows more extensive Li diffusion. With substantial Zr disorder ($T_{\text{eff}} = 5000$ K), the Li trajectories demonstrate interconnected diffusion pathways across Li sites, which rationalize the high Li mobility promoted by Zr disorder.

IV. DISCUSSION

In the realm of ASSBs, chloride-based lithium superionic conductors stand out because of their high ionic conductivity, interface stability, and oxidation resistance. Optimizing the Li migration barriers and increasing Li site connectivity are important roads for enhancing Li-ion conductivity in chloride-based solid-state electrolytes. Prior research has indicated relatively low energy barriers (< 0.3 eV) for lithium diffusion in both hcp and ccp frameworks of chlorides from either NEB calculations or by fitting the diffusivities derived from AIMD simulations at high temperatures [12]. However, the LZC synthesized by solid-state heating exhibits a much higher activation energy and lower Li-ion conductivity at room temperature than would be expected from these basic models. Ball-milled LZC, on the other hand, is more conductive.

We selected the LZC system as a representative model to elucidate the effect of cation disorder on ionic transport because it exists in both α - (hcp) and β - (fcc) phases, encompassing the typical anion arrangements common for closed-packed halide conductors. We quantified the degree of cation disorder within LZC by distinguishing between two key degrees of freedom: Li/vacancy disorder and Zr disorder. Our CE-MC simulations reveal three key findings: (1) no spontaneous Zr disorder is attainable through thermal fluctuations alone at any temperature reasonably accessible in solid-state synthesis, (2) thermal fluctuations at room temperature are inadequate to sustain Li/vacancy disorder when Zr is well-ordered in its ground state, and (3) Zr disorder frustrates the configurational energy landscape and enables facile Li/vacancy disorder at room temperature. These findings are supported by MLIP-MD (kinetic simulations), which reveal significant non-Arrhenius behavior of the Li diffusivity when Zr is well-ordered in contrast to the Zr-disordered states, which show typical Arrhenius behavior in the full temperature range. Using MLIP-MD, evidence

for non-Arrhenius behavior has also been shown for several other chloride compounds, such as Li_3YCl_6 [26] and $\text{Na}_{3-x}\text{Y}_{1-x}\text{Zr}_x\text{Cl}_6$ [58, 59], leading to reduced conductivities near room temperature.

Our simulations reveal that the β -LZC polymorph exhibits lower activation energy ($E_a = 0.68$ eV) than α -LZC ($E_a = 0.97$ eV) when Zr is fully ordered, and that β -LZC achieves an activation energy for Li-ion diffusion ($E_a = 0.31$ eV) similar to that of the highly disordered state even with partial Zr disorder. This suggests that the β -LZC structure type may serve as a better framework for achieving fast Li transport without necessitating complete cation disorder through high-energy ball milling. This is consistent with the experimental findings that doping β -LZC with Sc/In leading to partial cation occupancy, even via solid-state heating, can achieve Li-ion conductivities over 2 mS/cm [19, 20]

In summary, our study identifies metal disorder as a critical determinant for achieving high Li transport in halide superionic conductors. In Li_2ZrCl_6 , the high effective temperature required for Zr disorder limits equilibrium pathways for its synthesis and highlights the importance of manipulating cation disorder through non-equilibrium synthesis strategies. As many such non-equilibrium synthesis approaches are often more expensive and less scalable, in particular given the air sensitivity of these materials, novel strategies, including structural or chemical modifications may be required. The application of doping strategies or the exploration of high-entropy approaches may serve as viable pathways to introduce cation disorder, thereby promoting the configurational entropy to facilitate the Li/vacancy disorder [60]. Finally, given the importance of metal disorder for Li transport, it may be required to better understand if such disorder remains thermally stable over the typical lifetimes expected for battery materials.

V. ACKNOWLEDGMENTS

This work was supported by the Assistant Secretary for Energy Efficiency and Renewable Energy, Vehicle Technologies Office, under the Advanced Battery Materials Research (BMR) Program, of the U.S. Department of Energy under Contract No. DE-AC02-05CH11231. The computational modeling in this work was supported by the computational resources provided by the Extreme Science and Engineering Discovery Environment (XSEDE), supported by National Science Foundation grant number ACI1053575; the National Energy Research Scientific Computing Center (NERSC); and the National Renewable Energy Laboratory (NREL) clusters under ahlssc allocation. The authors thank Xiaochen Yang for valuable discussions and Yu Xie for the help on the Flare package setups.

- [1] J. Janek and W. G. Zeier, A solid future for battery development, *Nature Energy* **1**, 16141 (2016).
- [2] S. Xia, X. Wu, Z. Zhang, Y. Cui, and W. Liu, Practical challenges and future perspectives of all-solid-state lithium-metal batteries, *Chem* **5**, 753 (2019).
- [3] Y.-K. Sun, Promising all-solid-state batteries for future electric vehicles, *ACS Energy Letters* **5**, 3221 (2020).
- [4] X. Li, J. Liang, X. Yang, K. R. Adair, C. Wang, F. Zhao, and X. Sun, Progress and perspectives on halide lithium conductors for all-solid-state lithium batteries, *Energy & Environmental Science* **13**, 1429 (2020).
- [5] C. Wang, J. Liang, J. T. Kim, and X. Sun, Prospects of halide-based all-solid-state batteries: From material design to practical application, *Science Advances* **8**, eadc9516 (2022).
- [6] H. Kwak, S. Wang, J. Park, Y. Liu, K. T. Kim, Y. Choi, Y. Mo, and Y. S. Jung, Emerging halide superionic conductors for all-solid-state batteries: Design, synthesis, and practical applications, *ACS Energy Letters* **7**, 1776 (2022).
- [7] B. Helm, R. Schlem, B. Wankmiller, A. Banik, A. Gautam, J. Ruhl, C. Li, M. R. Hansen, and W. G. Zeier, Exploring Aliovalent Substitutions in the Lithium Halide Superionic Conductor $\text{Li}_{3-x}\text{In}_{1-x}\text{Zr}_x\text{Cl}_6$ ($0 \leq x \leq 0.5$), *Chemistry of Materials* **33**, 4773 (2021).
- [8] R. Schlem, A. Banik, S. Ohno, E. Suard, and W. G. Zeier, Insights into the Lithium Sub-structure of Superionic Conductors Li_3YCl_6 and Li_3YBr_6 , *Chemistry of Materials* **33**, 327 (2021).
- [9] L. Zhou, T.-T. Zuo, C. Y. Kwok, S. Y. Kim, A. Assoud, Q. Zhang, J. Janek, and L. F. Nazar, High areal capacity, long cycle life 4 V ceramic all-solid-state Li-ion batteries enabled by chloride solid electrolytes, *Nature Energy* **7**, 83 (2022).
- [10] L. Zhou, T. Zuo, C. Li, Q. Zhang, J. Janek, and L. F. Nazar, $\text{Li}_{3-x}\text{Zr}_x(\text{Ho}/\text{Lu})_{1-x}\text{Cl}_6$ Solid Electrolytes Enable Ultrahigh-Loading Solid-State Batteries with a Prelithiated Si Anode, *ACS Energy Letters* **8**, 3102 (2023).
- [11] T. Asano, A. Sakai, S. Ouchi, M. Sakaida, A. Miyazaki, and S. Hasegawa, Solid halide electrolytes with high lithium-ion conductivity for application in 4 V class bulk-type all-solid-state batteries, *Advanced Materials* **30**, 1803075 (2018).
- [12] S. Wang, Q. Bai, A. M. Nolan, Y. Liu, S. Gong, Q. Sun, and Y. Mo, Lithium chlorides and bromides as promising solid-state chemistries for fast ion conductors with good electrochemical stability, *Angewandte Chemie International Edition* **58**, 8039 (2019).
- [13] Y. Xiao, Y. Wang, S.-H. Bo, J. C. Kim, L. J. Miara, and G. Ceder, Understanding interface stability in solid-state batteries, *Nature Reviews Materials* **5**, 105 (2020).
- [14] W. D. Richards, L. J. Miara, Y. Wang, J. C. Kim, and G. Ceder, Interface Stability in Solid-State Batteries, *Chemistry of Materials* **28**, 266 (2016).
- [15] Y. Zhu and Y. Mo, Materials Design Principles for Air-Stable Lithium/Sodium Solid Electrolytes, *Angewandte Chemie* **132**, 17625 (2020).
- [16] K. Wang, Q. Ren, Z. Gu, C. Duan, J. Wang, F. Zhu, Y. Fu, J. Hao, J. Zhu, L. He, C.-W. Wang, Y. Lu, J. Ma, and C. Ma, A cost-effective and humidity-tolerant chloride solid electrolyte for lithium batteries, *Nature Communications* **12**, 4410 (2021).
- [17] H. Kwak, D. Han, J. Lyoo, J. Park, S. H. Jung, Y. Han, G. Kwon, H. Kim, S.-T. Hong, K.-W. Nam, *et al.*, New Cost-Effective Halide Solid Electrolytes for All-Solid-State Batteries: Mechanochemically Prepared Fe^{3+} -Substituted Li_2ZrCl_6 , *Advanced Energy Materials* **11**, 2003190 (2021).
- [18] F. Li, X. Cheng, L.-L. Lu, Y.-C. Yin, J.-D. Luo, G. Lu, Y.-F. Meng, H. Mo, T. Tian, J.-T. Yang, W. Wen, Z.-P. Liu, G. Zhang, C. Shang, and H.-B. Yao, Stable All-Solid-State Lithium Metal Batteries Enabled by Machine Learning Simulation Designed Halide Electrolytes, *Nano Letters* **22**, 2461 (2022).
- [19] H. Kwak, D. Han, J. P. Son, J. S. Kim, J. Park, K. W. Nam, H. Kim, and Y. S. Jung, Li^+ conduction in aliovalent-substituted monoclinic $\text{Li}_{2+x}\text{Zr}_{1-x}\text{M}_x\text{Cl}_6$ ($\text{M} = \text{In}, \text{Sc}$), *Chemical Engineering Journal* **437** (2022).
- [20] W. Li, Z. Chen, Y. Chen, W. Duan, G. Liu, Y. Lv, H. Yang, and L. Yao, High-voltage superionic and humidity-tolerant $\text{Li}_{2.5}\text{Sc}_{0.5}\text{Zr}_{0.5}\text{Cl}_6$ conductor for lithium batteries via preferred orientation, *Chemical Engineering Journal* **455**, 140509 (2023).
- [21] S. Chen, C. Yu, C. Wei, Z. Jiang, Z. Zhang, L. Peng, S. Cheng, and J. Xie, Unraveling Electrochemical Stability and Reversible Redox of Y-Doped Li_2ZrCl_6 Solid Electrolytes, *Energy Material Advances* **4**, 4 (2023).
- [22] J. Shi, Z. Yao, J. Xiang, C. Cai, F. Tu, Y. Zhang, W. Yao, Q. Jia, Y. Zhou, S. Shen, and Y. Yang, High-Conductivity Li_2ZrCl_6 Electrolytes via an Optimized Two-Step Ball-Milling Method for All-Solid-State Lithium-Metal Batteries, *ACS Sustainable Chemistry & Engineering* **12**, 2009 (2024).
- [23] D. A. Kitchaev, Z. Lun, W. D. Richards, H. Ji, R. J. Clément, M. Balasubramanian, D.-H. Kwon, K. Dai, J. K. Papp, T. Lei, B. D. McCloskey, W. Yang, J. Lee, and G. Ceder, Design principles for high transition metal capacity in disordered rocksalt Li-ion cathodes, *Energy & Environmental Science* **11**, 2159 (2018).
- [24] Z. Lun, B. Ouyang, Z. Cai, R. J. Clément, D.-H. Kwon, J. Huang, J. K. Papp, M. Balasubramanian, Y. Tian, B. D. McCloskey, H. Ji, H. Kim, D. A. Kitchaev, and G. Ceder, Design Principles for High-Capacity Mn-Based Cation-Disordered Rocksalt Cathodes, *Chem* **6**, 153 (2020).
- [25] R. Schlem, S. Muy, N. Prinz, A. Banik, Y. Shao-Horn, M. Zobel, and W. G. Zeier, Mechanochemical Synthesis: A Tool to Tune Cation Site Disorder and Ionic Transport Properties of Li_3MCl_6 ($\text{M} = \text{Y}, \text{Er}$) Superionic Conductors, *Advanced Energy Materials* **10**, 1 (2020).
- [26] S. Wang, Y. Liu, and Y. Mo, Frustration in Superionic Conductors Unraveled by the Density of Atomistic States, *Angewandte Chemie* **135** (2023).
- [27] E. Sebti, H. A. Evans, H. Chen, P. M. Richardson, K. M. White, R. Giovine, K. P. Koirala, Y. Xu, E. Gonzalez-Correa, C. Wang, C. M. Brown, A. K. Cheetham, P. Canepa, and R. J. Clément, Stacking Faults Assist Lithium-Ion Conduction in a Halide-Based Superionic Conductor, *Journal of the American Chemical Society* **144**, 5795 (2022).

- [28] J. Liang, X. Li, S. Wang, K. R. Adair, W. Li, Y. Zhao, C. Wang, Y. Hu, L. Zhang, S. Zhao, S. Lu, H. Huang, R. Li, Y. Mo, and X. Sun, Site-Occupation-Tuned Superionic $\text{Li}_x\text{ScCl}_{3+x}$ Halide Solid Electrolytes for All-Solid-State Batteries, *Journal of the American Chemical Society* **142**, 7012 (2020).
- [29] S. Yu, J. Noh, B. Kim, J.-h. Song, K. Oh, J. Yoo, S. Lee, S.-O. Park, W. Kim, B. Kang, D. Kil, and K. Kang, Design of a trigonal halide superionic conductor by regulating cation order-disorder, *Science* **382**, 573 (2023).
- [30] J. Sanchez, F. Ducastelle, and D. Gratias, Generalized cluster description of multicomponent systems, *Physica A: Statistical Mechanics and its Applications* **128**, 334 (1984).
- [31] C. Wolverton and A. Zunger, First-principles prediction of vacancy order-disorder and intercalation battery voltages in Li_xCoO_2 , *Physical Review Letters* **81**, 606 (1998).
- [32] P. Zhong, F. Xie, L. Barroso-Luque, L. Huang, and G. Ceder, Modeling Intercalation Chemistry with Multi-redox Reactions by Sparse Lattice Models in Disordered Rocksalt Cathodes, *PRX Energy* **2**, 043005 (2023).
- [33] Z. Deng, G. Sai Gautam, S. K. Kolli, J.-N. Chotard, A. K. Cheetham, C. Masquelier, and P. Canepa, Phase Behavior in Rhombohedral NaSiCON Electrolytes and Electrodes, *Chemistry of Materials* **32**, 7908 (2020).
- [34] R. L. Kam, K. Jun, L. Barroso-Luque, J. H. Yang, F. Xie, and G. Ceder, Crystal Structures and Phase Stability of the $\text{Li}_2\text{S-P}_2\text{S}_5$ System from First Principles, *Chemistry of Materials* **35**, 9111 (2023).
- [35] J. H. Yang, T. Chen, L. Barroso-Luque, Z. Jadidi, and G. Ceder, Approaches for handling high-dimensional cluster expansions of ionic systems, *npj Computational Materials* **8**, 133 (2022).
- [36] P. Zhong, T. Chen, L. Barroso-Luque, F. Xie, and G. Ceder, An $\ell_0\ell_2$ -norm regularized regression model for construction of robust cluster expansions in multicomponent systems, *Physical Review B* **106**, 024203 (2022).
- [37] W. Huang, A. Urban, Z. Rong, Z. Ding, C. Luo, and G. Ceder, Construction of ground-state preserving sparse lattice models for predictive materials simulations, *npj Computational Materials* **3**, 30 (2017).
- [38] Gurobi Optimization, LLC, Gurobi Optimizer Reference Manual (2021).
- [39] L. Barroso-Luque, P. Zhong, J. H. Yang, F. Xie, T. Chen, B. Ouyang, and G. Ceder, Cluster expansions of multicomponent ionic materials: Formalism and methodology, *Physical Review B* **106**, 144202 (2022).
- [40] L. Barroso-Luque, J. H. Yang, F. Xie, T. Chen, R. L. Kam, Z. Jadidi, P. Zhong, and G. Ceder, smol: A Python package for cluster expansions and beyond, *Journal of Open Source Software* **7**, 4504 (2022).
- [41] S. P. Ong, W. D. Richards, A. Jain, G. Hautier, M. Kocher, S. Cholia, D. Gunter, V. L. Chevrier, K. A. Persson, and G. Ceder, Python Materials Genomics (pymatgen): A robust, open-source python library for materials analysis, *Computational Materials Science* **68**, 314 (2013).
- [42] B. Deng, P. Zhong, K. Jun, J. Riebesell, K. Han, C. J. Bartel, and G. Ceder, CHGNet as a pretrained universal neural network potential for charge-informed atomistic modelling, *Nature Machine Intelligence* **5**, 1031 (2023).
- [43] J. Sun, A. Ruzsinszky, and J. P. Perdew, Strongly Constrained and Appropriately Normed Semilocal Density Functional, *Physical Review Letters* **115**, 036402 (2015).
- [44] J. W. Furness, A. D. Kaplan, J. Ning, J. P. Perdew, and J. Sun, Accurate and Numerically Efficient $r^2\text{SCAN}$ Meta-Generalized Gradient Approximation, *The Journal of Physical Chemistry Letters* **11**, 8208 (2020).
- [45] G. Kresse and J. Furthmüller, Efficiency of ab-initio total energy calculations for metals and semiconductors using a plane-wave basis set, *Computational Materials Science* **6**, 15 (1996).
- [46] G. Kresse and D. Joubert, From ultrasoft pseudopotentials to the projector augmented-wave method, *Physical Review B* **59**, 1758 (1999).
- [47] S. Batzner, A. Musaelian, L. Sun, M. Geiger, J. P. Mailoa, M. Kornbluth, N. Molinari, T. E. Smidt, and B. Kozinsky, E(3)-equivariant graph neural networks for data-efficient and accurate interatomic potentials, *Nature Communications* **13**, 2453 (2022).
- [48] C. Chen and S. P. Ong, A universal graph deep learning interatomic potential for the periodic table, *Nature Computational Science* **2**, 718 (2022).
- [49] J. Qi, S. Banerjee, Y. Zuo, C. Chen, Z. Zhu, M. L. Holekevi Chandrappa, X. Li, and S. P. Ong, Bridging the gap between simulated and experimental ionic conductivities in lithium superionic conductors, *Materials Today Physics* **21** (2021).
- [50] J. P. Perdew, K. Burke, and M. Ernzerhof, Generalized gradient approximation made simple, *Physical review letters* **77**, 3865 (1996).
- [51] S. Grimme, J. Antony, S. Ehrlich, and H. Krieg, A consistent and accurate ab initio parametrization of density functional dispersion correction (dft-d) for the 94 elements h-pu, *The Journal of chemical physics* **132** (2010).
- [52] J. Vandermause, Y. Xie, J. S. Lim, C. J. Owen, and B. Kozinsky, Active learning of reactive Bayesian force fields applied to heterogeneous catalysis dynamics of H/Pt, *Nature Communications* **13**, 5183 (2022).
- [53] Y. Xie, J. Vandermause, S. Ramakers, N. H. Protik, A. Johansson, and B. Kozinsky, Uncertainty-aware molecular dynamics from Bayesian active learning for phase transformations and thermal transport in SiC, *npj Computational Materials* **9**, 36 (2023).
- [54] H. J. Berendsen, J. v. Postma, W. F. Van Gunsteren, A. DiNola, and J. R. Haak, Molecular dynamics with coupling to an external bath, *The Journal of Chemical Physics* **81**, 3684 (1984).
- [55] X. He, Y. Zhu, A. Epstein, and Y. Mo, Statistical variances of diffusional properties from ab initio molecular dynamics simulations, *npj Computational Materials* **4**, 18 (2018).
- [56] A. H. Larsen, J. J. Mortensen, J. Blomqvist, I. E. Castelli, R. Christensen, M. Dulak, J. Friis, M. N. Groves, B. Hammer, C. Hargus, *et al.*, The atomic simulation environment—a Python library for working with atoms, *Journal of Physics: Condensed Matter* **29**, 273002 (2017).
- [57] P. D. Tapesch, G. D. Garbulsky, and G. Ceder, Model for Configurational Thermodynamics in Ionic Systems, *Physical Review Letters* **74**, 2272 (1995).
- [58] E. A. Wu, S. Banerjee, H. Tang, P. M. Richardson, J.-M. Doux, J. Qi, Z. Zhu, A. Grenier, Y. Li, E. Zhao, G. Deysher, E. Sebti, H. Nguyen, R. Stephens, G. Verbist, K. W. Chapman, R. J. Clément, A. Banerjee, Y. S. Meng, and S. P. Ong, A stable cathode-solid electrolyte composite for high-voltage, long-cycle-life solid-state sodium-ion batteries, *Nature Communications* **12**,

- 1256 (2021).
- [59] E. Sebtı, J. Qi, P. M. Richardson, P. Ridley, E. A. Wu, S. Banerjee, R. Giovine, A. Cronk, S.-Y. Ham, Y. S. Meng, S. P. Ong, and R. J. Clément, Synthetic control of structure and conduction properties in Na–Y–Zr–Cl solid electrolytes, *Journal of Materials Chemistry A* **10**, 21565 (2022).
- [60] Y. Zeng, B. Ouyang, J. Liu, Y.-W. Byeon, Z. Cai, L. J. Miara, Y. Wang, and G. Ceder, High-entropy mechanism to boost ionic conductivity, *Science* **378**, 1320 (2022).